Design and Validation of a Course Control System for a Wave-Propelled Unmanned Surface Vehicle

Alberto Dallolio[*], Henning Øveraas[*], Jo A. Alfredsen[*], Thor I. Fossen[*], Tor A. Johansen[*]
Centre for Autonomous Marine Operations and Systems, Department of Engineering Cybernetics
Norwegian University of Science and Technology (NTNU), Trondheim, Norway

Abstract

Unlike common marine vessels, wave-propelled vehicles cannot directly control their speed, but rely instead on the forces exerted by the environment to navigate as intended. The unique navigation capabilities of such vehicles motivate the study of control solutions that adapt the vehicle heading to the prevailing environmental conditions and ensure robust course-keeping performances across different sea states, winds and currents over extended periods of time. This article presents the design and experimental validation of a path following and course control system for an underactuated, wave-propelled unmanned surface vehicle (USV). The major focus and novelty of this work stands in the analysis of the model nonlinearities that appear when the vehicle propulsion force does not prevail on the wind and sea current forces generated by the environment. In these situations, low maneuverability is experienced depending on the magnitude of counteracting forces and, in some cases, loss of controllability is a risk. Initial investigation of the vehicle's nonlinear dynamics is followed by derivation of a simplified quasi-linear mathematical model that isolates the major source of nonlinearity. This provides a basis for the control design, whose theory is supported and validated by extensive field experiments. In particular, when the USV's ground speed is close to zero, the theory shows singularities in the model that lead to instabilities and loss of controllability of the course over ground that is experienced in the field. Our test results verify that an effective solution is to switch to heading control when the ground speed is small.

Keywords: Autonomous Surface Vehicles, Control application, Robotics, Experimental results.

1 Introduction

Ocean dynamics and environmental phenomena are nowadays characterized by fast rates of evolution that represent a huge threat to biodiversity. Observing rapid environmental changes has become a necessity, and to do so by moving towards persistent and sustainable ocean monitoring. To date, science-driven oceanic exploration and observation of the upper water column by means of robotic systems have already been demonstrated (Ferreira et al., 2019; Costa and et.al, 2018; McGillivary et al., 2012; Cross et al., 2015). Nevertheless, current ocean monitoring efforts either rely on robotic platforms or on ship-based observations as a supplement to remote sensing. Whereas ship-based monitoring is not sustainable and cannot scale across

[*]{alberto.dallolio,henning.overaas,jo.arve.alfredsen,thor.fossen,tor.arne.johansen}@ntnu.no

space and time, the vast majority of current mobile robotic platforms are heavily constrained by proximity to shore or to a support vessel, Lagrangian motion, limited payload and onboard energy.

The employment of surface and underwater gliders in the study of environmental phenomena is nowadays consolidated (Camus et al., 2019). Several long-endurance, green energy surface vehicles are available on the market, e.g., Liquid Robotics WaveGlider (Manley and Willcox, 2010), Offshore Sensing SailBuoy (Fer and Peddie, 2013), AutoNaut (Johnston and Poole, 2017), or L3 Technologies C-Enduro Technologies (2019). Unlike common marine platforms, these vehicles are less constrained by energy limitations with respect to both payload usage and propulsion, ensuring long-duration missions without physical human intervention (Manley and Willcox, 2010). As a consequence, the guidance, navigation and control (GNC) systems implemented onboard these vehicles need to show a degree of robustness that is high enough to allow sustained autonomous operations across different sea states, winds and currents, and for extended periods of time (e.g., in the order of weeks). However, this comes with several limitations that mainly affect the vehicle maneuverability. Most often, the speed (over ground and through water) of the vehicle is not controllable and therefore, in order to predict future vehicle's states, one must rely on estimates based on present and forecasted sea states, winds and ocean currents. Stable course over ground control can also be a challenge whenever the forces exerted by the environment predominate on their steering and propulsion forces, and prevent them from achieving an intended behavior. The maneuverability limitations due to adverse environmental forces cannot be addressed with common navigation and control techniques, which rely on the ability of motored propulsion to firmly govern the behavior of the vehicle. Course-keeping autopilots are usually designed using classical linear control theory, based on basic models such as the classical Nomoto model (Nomoto, 1957) that neglects the effect of environmental forces and simply relies on integral action (Fossen, 2021). For vehicles that have a large variation in speed, the nonlinear effects of speed are often handled using gain-scheduled control. Autonomous underwater vehicles instead, may use heading control rather than course control since accurate heading measurements are more easily available under water than accurate course-over-ground measurements, as described in Fossen (2021). Course control of a different wave-propelled USV using linear control theory is addressed in Wang et al. (2019). That work is however developed for the Wave Glider (Hine et al., 2009), a multi-body unmanned platform that is significantly different from the one considered in this article since the propulsion and steering force generating underwater body is tethered (i.e., not rigidly attached) to the surface hull. Despite being focused on modeling the speed, Smith et al. (2011) and Bowker et al. (2020) show relevant modeling approaches for the Wave Glider.

The literature lacks detailed mathematical analyses of how control systems onboard the aforementioned platforms can cope with environmental forces that are in the same order of magnitude as their propulsion capabilities. We therefore describe the dynamic modeling and course control of wave-propelled USVs taking into account the relevant effects of ocean current and other environmental forces that may lead to very low speed-over-ground. When removing this assumption, we must consider singularities at zero ground speed that are generally not considered in the course-keeping control of marine vehicles with motorized propulsion that can avoid these conditions. The models give insight into the changes in steering dynamics as a function of changing environmental conditions, which is exploited in the control design to handle singular situations that occur when the speed-over-ground approaches zero. Although the singularity as zero ground speed invalidates the common assumption of linearity of the course-keeping model, we show that classical control design principles based on robust linear course and heading control can still be applied by switching to heading control at low ground speed. The main contribution of the paper is the underlying model analysis and field experimental validation. The controller has been operational and tested at several sites both in the open ocean and coastal environments for about 7 weeks in total, in periods with waves of about 5 meters height, winds up to 25 m/s and strong currents. We employ a 5-meter version (Figure 1) of the commercially available AutoNaut (Johnston and Poole, 2017), in which navigation, communication and payload control systems are designed and developed by the Norwegian University of Science and Technology (NTNU) as described in Dallolio et al. (2019).
This article is organized as follows. Section 2 introduces the experimental platform, the AutoNaut, and derives its nonlinear dynamic model (Section 2.1) and steering model (Section 2.2). A quasi-linear approximation is derived in Section 3.1. The quasi-linear model is analysed in the same chapter (Section 3.2), leading to a linear robust control design. Field experimental results are presented in Section 4, where the

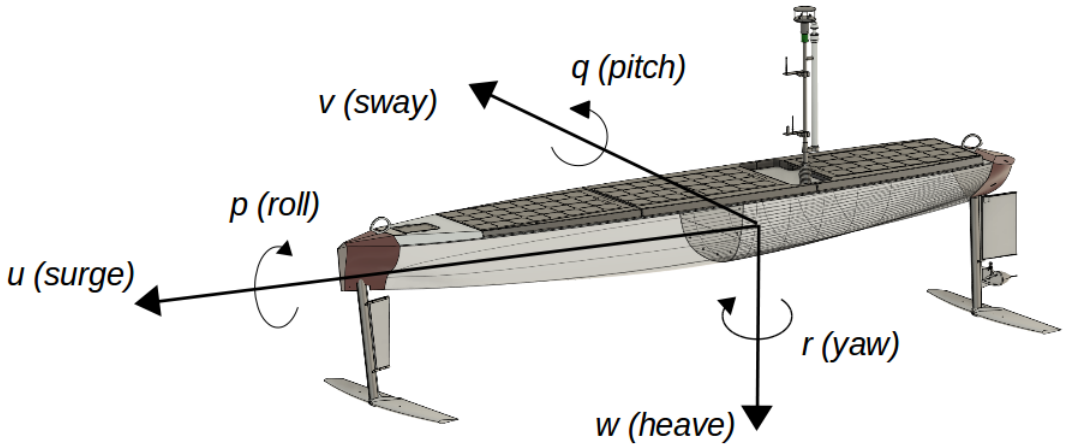

Figure 1: NTNU AutoNaut 3D model with body-fixed reference frame. Vertical struts at the vehicle's bow and aft end with symmetrical spring-loaded hydrofoils, main source of its propulsion.

proposed control methods are tested in mild (Section 4.1) and in adverse (Section 4.2) weather conditions. Model validation in both open and closed loop is finally presented in Section 4.3 before conclusions are presented in Section 5.

2 Theory

The AutoNaut (Figure 1) is an USV equipped with an innovative propulsion system that mainly relies on the heave and pitch motions caused by sea surface waves to produce forward thrust. This makes the platform suitable for sustained operations in the open ocean without human intervention. Besides, surface currents, second-order wave effects and winds generate forces that influence the speed and course over ground of the vehicle.

The vehicle is equipped with a passive submerged mechanism that transforms the motion generated by surface waves into forward propulsion (Bowker et al., 2015). Two pairs of underwater hydrofoils, spring-loaded to vertical struts bow and stern, provide forward thrust when the vehicle is pitched by surface waves. This mechanism generates forward speed up to 3 knots depending on both sea conditions and on the vehicle's heading relative to the wave direction. Heading or course over ground are controlled by a rudder placed on the rear strut as shown in Figure 1. The rudder angle $\delta \in [-45°, +45°]$ is commanded by the control unit placed in the front watertight compartment. Additionally, a small thruster is placed underneath the rudder. The thruster is intended to increase vehicle maneuverability and speed in confined waters (e.g., ports, bays) and during emergency situation (e.g., collision avoidance, complete loss of control). Its use is however as limited as possible due to the high demand of electric power. The publicly available design[1] and the validation of the overall control system architecture of the USV employed in this work are presented in Dallolio et al. (2019).

The USV speed relative to its surrounding water is mainly determined by surface currents, waves, and wind direction and speed. Speed drops are commonly observed when currents from starboard or port side prevent the vehicle from gliding on top of the waves or when strong winds and surface currents oppose to the vehicle's forward motion. Forces applied to the vehicle's sides also influence course-keeping performances, resulting in low controllability situations when the magnitude of environmental forces exceeds that generated by the propulsion system. In order to understand the control problem and the vehicle's inherent performance limitations, both a mathematical model analysis and field experiments are used.

[1] http://autonaut.itk.ntnu.no/doku.php

2.1 Nonlinear dynamic model

Typically, the speed over ground (SOG) achieved by a wave-propelled USV is in the range of 0-3 knots depending on the sea state and the ocean currents and wind. This implies that the vehicle's speed is of the same order of magnitude as the ocean currents, which must therefore be considered in the model and the course control algorithm. The common approach of relying on integral action to deal with the ocean current and second-order wave forces by viewing them as a slowly time-varying disturbance may still be highly useful and necessary, but the nonlinearities and couplings in the USV dynamics should also be addressed.
Consider the 3-degrees of freedom rigid body and hydrodynamic vehicle model for the horizontal plane (Fossen, 2021)

$$M\dot{\boldsymbol{\nu}}_r + C(\boldsymbol{\nu}_r)\boldsymbol{\nu}_r + D(\boldsymbol{\nu}_r)\boldsymbol{\nu}_r = \boldsymbol{\tau}, \tag{1}$$

where $M = M_A + M_{RB}$ accounts for rigid body and hydrodynamic added mass, $C(\boldsymbol{\nu}_r) = C_A(\boldsymbol{\nu}_r) + C_{RB}(\boldsymbol{\nu}_r)$ accounts for Coriolis and centripetal terms, and $D(\boldsymbol{\nu}_r)$ includes damping terms. In this representation $\boldsymbol{\nu}_r$ is the velocity vector of the vehicle relative to the ocean current. The vector $\boldsymbol{\tau}$ contains forces in surge and sway, and the corresponding yaw moment, generated by winds, waves, steering and propulsion mechanisms. Expanding the matrices in Equation (1) we obtain

$$M = \begin{pmatrix} m + A_{11} & 0 & 0 \\ 0 & m + A_{22} & 0 \\ 0 & 0 & J_z + A_{66} \end{pmatrix}, \tag{2}$$

$$C(\boldsymbol{\nu}_r) = \begin{pmatrix} 0 & -mr & -A_{22}v_r \\ mr & 0 & A_{11}u_r \\ A_{22}v_r & -A_{11}u_r & 0 \end{pmatrix} \tag{3}$$

and

$$D = \begin{pmatrix} D_{11} & 0 & 0 \\ 0 & D_{22} & 0 \\ 0 & 0 & D_{66} \end{pmatrix}. \tag{4}$$

We have used the following notation:

- m is the rigid-body vehicle mass;
- $r = \dot{\psi}$ is the yaw angular rate, where the yaw (heading) angle is denoted by ψ;
- u and v are the longitudinal and lateral components of the speed over ground (SOG), respectively, decomposed in the vehicle's body coordinate frame, such that $SOG = U = \sqrt{u^2 + v^2}$
- u_c and v_c are the longitudinal and lateral components of the ocean current velocity vector, respectively, decomposed in the vehicle's body coordinate frame. The current is assumed to be irrotational such that $r_c = 0$;
- $u_r = u - u_c$ and $v_r = v - v_c$ are the longitudinal and lateral components of the relative velocity, respectively, decomposed in the vehicle's body coordinate frame; $\boldsymbol{\nu}_r = [u_r, v_r, r]^T$
- J_z is the moment of inertia about the vertical axis;
- A_{ij} are hydrodynamic added mass and moment of inertia coefficients;
- D_{ij} are linear hydrodynamic damping coefficients;
- F_X and F_Y are the longitudinal and lateral steering and propulsion forces acting on the vehicle body, respectively, and τ_Z is the corresponding moment about the vertical axis acting on the vehicle body; $\boldsymbol{\tau} = [F_X, F_Y, \tau_Z]^T$.

The damping can be modeled using linear skin friction, quadratic surge resistance, and cross-flow drag in sway and yaw, see Fossen (2021) for details. Since the USV's ground speed is low, the quadratic damping in surge and the cross-flow drag can be linearized. The off-diagonal damping terms are set to zero since they are negligible at low speed. In fact, the linear coupling terms will be less than 5 % of its diagonal counterparts if the method of Clarke et al. (1982) is applied. The parameters of the system matrices M, C and D for the AutoNaut are presented in Appendix A.

By assuming that the ocean current is stationary and irrotational in the inertial coordinate system, a rotation with the vehicle's yaw angle should be used to define (u_c, v_c). Note that since the vector (u_c, v_c) is decomposed in the body frame, we have that $\dot{u}_c = v_c r$ and $\dot{v}_c = -u_c r$. Moreover, $U = \sqrt{u^2 + v^2}$ and $U_r = \sqrt{u_r^2 + v_r^2}$ are the USV's velocities relative to ground and to the water flow, respectively.

The course angle $\chi = \psi + \beta$ depends on the crab angle $\beta = \arctan(v/u) = \arcsin(v/U)$. Hence, the course angle dynamics can be expressed as

$$\begin{aligned} \dot{\chi} &= r + \frac{1}{1 + \frac{v^2}{u^2}} \frac{d}{dt}\left(\frac{v}{u}\right) \\ &= r + \frac{1}{U^2}(\dot{v}u - \dot{u}v). \end{aligned} \tag{5}$$

The expressions for $\dot{u}$ and $\dot{v}$ can be obtained from the vehicle's dynamics given by Equation (1):

$$\dot{u} = r v_c + \frac{m + A_{22}}{m + A_{11}} v_r r - \frac{D_{11}}{m + A_{11}} u_r + \frac{1}{m + A_{11}}(F_X + F_{Xw}) \tag{6}$$

$$\dot{v} = -r u_c - \frac{m + A_{11}}{m + A_{22}} u_r r - \frac{D_{22}}{m + A_{22}} v_r + \frac{1}{m + A_{22}}(F_Y + F_{Yw}) \tag{7}$$

$$\dot{r} = -\frac{D_{66}}{J_z + A_{66}} r - \frac{A_{22} - A_{11}}{J_z + A_{66}} u_r v_r + \frac{1}{J_z + A_{66}}(\tau_Z + N_{Zw}) \tag{8}$$

where we define F_X, F_Y and τ_Z as

$$F_X := F_{prop} + F_{XR} \tag{9}$$

$$F_Y := F_{YR} \tag{10}$$

$$\tau_Z := N_{ZR}. \tag{11}$$

Here we assume that the propulsion force generated by the submerged hydrofoils mechanism only affects the surge dynamics. F_{XR}, F_{YR} and N_{ZR} are respectively longitudinal and lateral horizontal forces, and yaw moment, generated by the rudder. F_{Xw}, F_{Yw} and N_{Zw} are longitudinal and lateral horizontal forces, and yaw moment, generated by the wind. While the steering model is discussed in the next section, we refer to Appendix A.2 for the wind model. Moreover, we refer to Appendix B for the definition and diagram of wind and sea current relative directions.

In this article we show that a model of the longitudinal propulsion force generated by the submerged foils is not necessary for the design of a course-keeping autopilot that instead uses the longitudinal speed as a time-varying known (measured) variable.

2.2 Steering model

The steering model captures the dynamics of the rudder forces and moments given by F_{XR}, F_{YR} and N_{ZR}. The rudder normal force is expressed as (Kijima et al., 1990)

$$F_N = \frac{1}{2}\rho U_r^2 A_R C_N \sin(\alpha_R), \tag{12}$$

where A_R is the rudder area, U_r is the total relative speed as defined earlier, and

$$\alpha_R = \delta - \tan^{-1}\left(\frac{v_r}{u_r}\right) \tag{13}$$

is the relative angle between rudder and current (in body frame) angles. According to Fujii and Tsuda (1962), C_N can be computed by

$$C_N = \frac{6.13\Lambda}{\Lambda + 2.25}, \tag{14}$$

where $\Lambda = b^2/A_R$ is the rudder aspect ratio, where b is the rudder height and A_R is the rudder area. The rudder normal force F_N contributes to forces in surge and sway as

$$F_{XR} = -(1 - t_R)F_N \sin(\delta) \tag{15}$$
$$F_{YR} = -(1 + a_H)F_N \cos(\delta) \tag{16}$$

and to the yaw moment as

$$N_{ZR} = -(x_R + a_H x_H)F_N \cos(\delta), \tag{17}$$

where x_R is the longitudinal coordinate of the rudder position (approximately $-0.5L_{pp}$, where L_{pp} is the length between perpendiculars of the vehicle). The coefficient for additional drag t_R can be approximated according to (Matsumoto and Suemitsu, 1980)

$$1 - t_R = 0.28C_B + 0.55, \tag{18}$$

where C_B is the USV block coefficient. The coefficients a_H and x_H can be chosen according to Kijima et al. (1990).

3 Method

3.1 Simplified quasi-linear model

Assume the surge velocity u is constant. This may be reasonable when following straight paths in open ocean, but has limitations during fast heading changes and when operating closer to shore where currents may change quickly. In this section we neglect the wind forces, for simplicity. In this case the course angle dynamics becomes

$$\begin{aligned}
\dot{\chi} &= r + \frac{u}{U^2}\dot{v} \\
&= r + \frac{u}{U^2}\left(-ru_c - \frac{m + A_{11}}{m + A_{22}}u_r r - \frac{D_{22}}{m + A_{22}}v_r + \frac{1}{m + A_{22}}F_Y\right) \\
&= \gamma r + \frac{u}{U^2}\left(-\frac{D_{22}}{m + A_{22}}v_r + \frac{F_Y}{m + A_{22}}\right),
\end{aligned} \tag{19}$$

where

$$\gamma = 1 - \frac{u}{U^2}u_c - \frac{u}{U^2}\frac{m + A_{11}}{m + A_{22}}u_r. \tag{20}$$

Combining this with the lateral vehicle dynamics leads to the third order quasi-linear system

$$\begin{aligned}
\begin{pmatrix} \dot{\chi} \\ \dot{v} \\ \dot{r} \end{pmatrix} &= \begin{pmatrix} 0 & -\frac{u}{U^2}\frac{D_{22}}{m+A_{22}} & \gamma \\ 0 & -\frac{D_{22}}{m+A_{22}} & -u_c - \frac{m+A_{11}}{m+A_{22}}u_r \\ 0 & 0 & -\frac{D_{66}}{J_z+A_{66}} \end{pmatrix} \begin{pmatrix} \chi \\ v \\ r \end{pmatrix} \\
&\quad + \begin{pmatrix} \frac{u}{U^2}\frac{D_{22}}{m+A_{22}} \\ \frac{D_{22}}{m+A_{22}} \\ 0 \end{pmatrix} v_c - \begin{pmatrix} 0 \\ 0 \\ \frac{A_{22}-A_{11}}{J_z+A_{66}} \end{pmatrix} u_r v_r + \begin{pmatrix} \frac{u}{U^2}\frac{1}{m+A_{22}} & 0 \\ \frac{1}{m+A_{22}} & 0 \\ 0 & \frac{1}{J_z+A_{66}} \end{pmatrix} \begin{pmatrix} F_Y \\ \tau_Z \end{pmatrix},
\end{aligned} \tag{21}$$

whose equivalent formulation is:

$$\begin{pmatrix} \dot{\chi} \\ \dot{v}_r \\ \dot{r} \end{pmatrix} = \begin{pmatrix} 0 & -\frac{u}{U^2}\frac{D_{22}}{m+A_{22}} & \gamma \\ 0 & -\frac{D_{22}}{m+A_{22}} & -\frac{m+A_{11}}{m+A_{22}}u_r \\ 0 & -\frac{A_{22}-A_{11}}{J_z+A_{66}}u_r & -\frac{D_{66}}{J_z+A_{66}} \end{pmatrix} \begin{pmatrix} \chi \\ v_r \\ r \end{pmatrix} + \begin{pmatrix} \frac{u}{U^2}\frac{1}{m+A_{22}} & 0 \\ \frac{1}{m+A_{22}} & 0 \\ 0 & \frac{1}{J_z+A_{66}} \end{pmatrix} \begin{pmatrix} F_{YR} \\ N_{ZR} \end{pmatrix}. \quad (22)$$

The normal force generated by the rudder, Equation (12), can be rewritten as

$$F_N = \frac{1}{2}\rho U_r A_R C_N (u_r \sin(\delta) - v_r \cos(\delta)). \quad (23)$$

We further assume the rudder angle is small and make the approximations $\cos(\delta) \approx 1$ and $\sin(\delta) \approx \delta$. The lateral force and yaw moment given by Equations (16) and (17) then become

$$F_{YR} \approx -\frac{1}{2}(1+a_H)\rho U_r A_R C_N (u_r\delta - v_r) \quad (24)$$

$$N_{ZR} \approx -\frac{1}{2}(x_R + a_H x_H)\rho U_r A_R C_N (u_r\delta - v_r) \quad (25)$$

or equivalently

$$F_{YR} \approx \alpha_{YR} U_r (u_r\delta - v_r) \quad (26)$$

$$N_{ZR} \approx \alpha_{ZR} U_r (u_r\delta - v_r), \quad (27)$$

where $\alpha_{YR} = -\frac{1}{2}(1+a_H)\rho A_R C_N$ and $\alpha_{ZR} = -\frac{1}{2}(x_R + a_H x_H)\rho A_R C_N$. The simplified quasi-linear model corresponding to Equation (22) then becomes:

$$\begin{pmatrix} \dot{\chi} \\ \dot{v}_r \\ \dot{r} \end{pmatrix} = \begin{pmatrix} 0 & -\frac{u}{U^2}\frac{1}{m+A_{22}}(D_{22}+\alpha_{YR}U_r) & \gamma \\ 0 & -\frac{1}{m+A_{22}}(D_{22}+\alpha_{YR}U_r) & -\frac{m+A_{11}}{m+A_{22}}u_r \\ 0 & -\frac{1}{J_z+A_{66}}((A_{22}-A_{11})u_r + \alpha_{ZR}U_r) & -\frac{D_{66}}{J_z+A_{66}} \end{pmatrix} \begin{pmatrix} \chi \\ v_r \\ r \end{pmatrix} + \begin{pmatrix} \frac{u}{U^2}\frac{\alpha_{YR}U_r u_r}{m+A_{22}} \\ \frac{\alpha_{YR}U_r u_r}{m+A_{22}} \\ \frac{\alpha_{ZR}U_r u_r}{J_z+A_{66}} \end{pmatrix} \delta. \quad (28)$$

In the forthcoming we denote the transfer function resulting from this model $H_{ql}(s) = \frac{\chi}{\delta}(s)$.

3.2 Model analysis and control

We consider in this section the case in which the lateral dynamics is eliminated from the model in Equation (28) by discarding the second row and column of the third-order state-space model and the effects of F_{YR}. Assume that $u = u_c + u_{prop}$, where u_{prop} is an equivalent constant speed due to wave propulsion only. This leads to a second-order system that can easily be shown to correspond to the well-known and widely employed Nomoto model (Fossen, 2021) with a gain that depends on γ, u_{prop} and U_r:

$$H_n(s) = \frac{\chi}{\delta}(s) = \frac{\gamma u_{prop} U_r K}{s(1+Ts)}. \quad (29)$$

Consider first a nominal reference case where $u_{prop} = 1\ m/s$ and $u_c = v_c = 0$. The transfer function $H_{ql}(s)$ is shown in Figure 2. The figure also shows the transfer function of the Nomoto model (29) for comparison. It can be seen that the high-frequency gain is the same, but there is a difference in the gain at lower frequencies between 0 and +8 dB, while the phase difference is up to 40°. In order to understand how

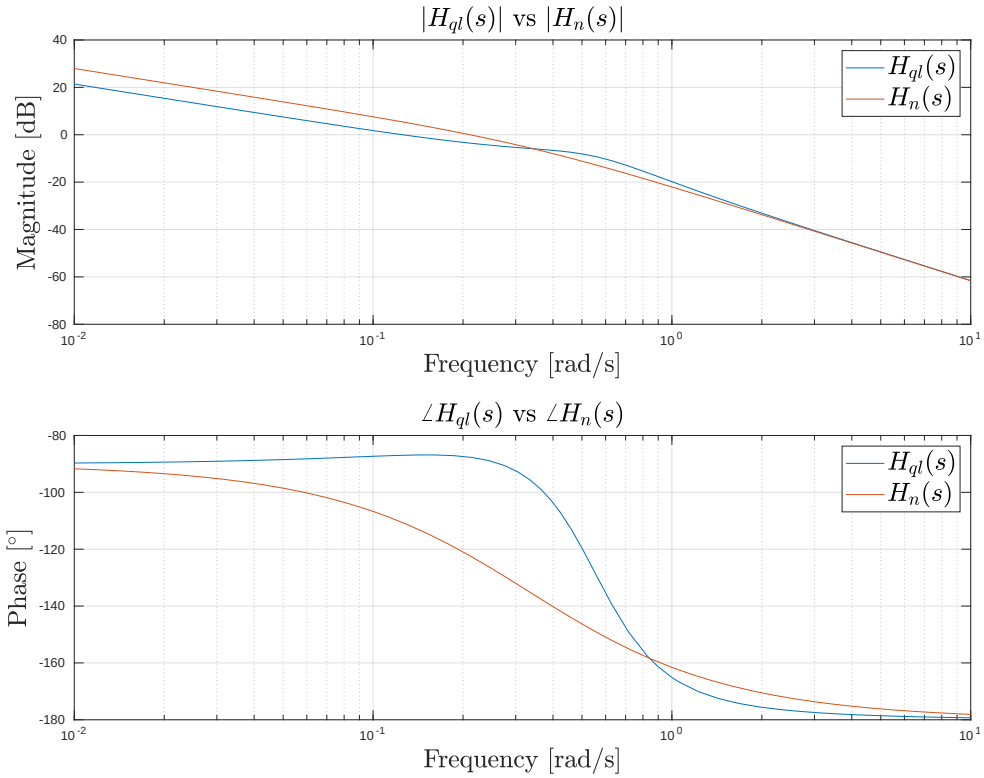

Figure 2: Transfer functions of quasi-linear third order model $H_{ql}(s)$ (red) and Nomoto model $H_n(s)$ (blue).

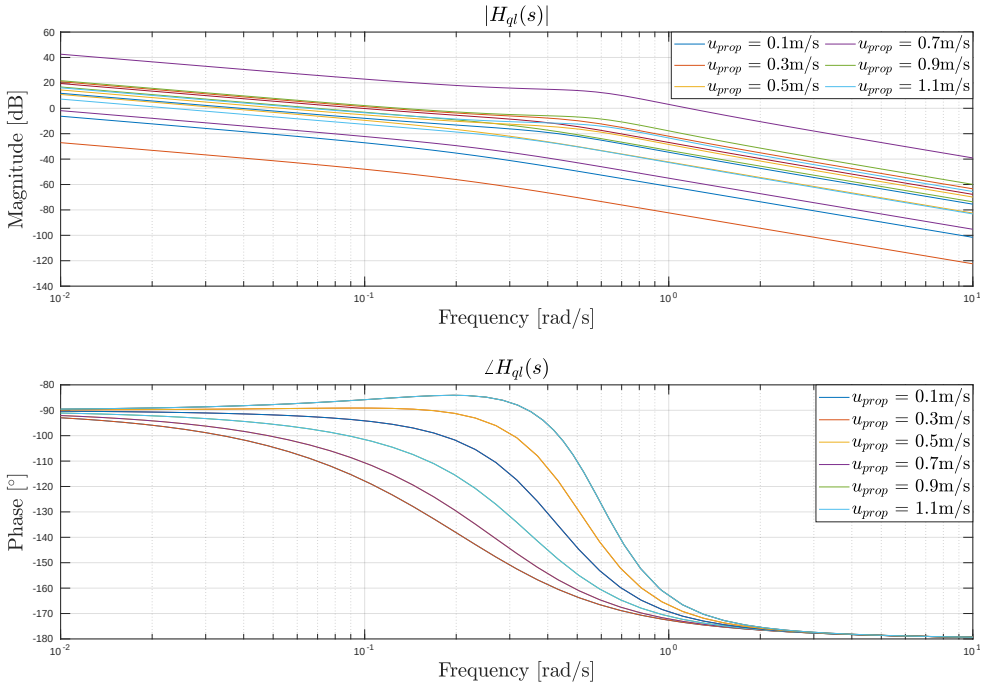

Figure 3: Transfer function $H_{ql}(s)$ from δ to χ for third-order quasi-linear model when $u_c \in [-1, 1]$ m/s and $u_{prop} \in [0.1, 1.1]$ m/s.

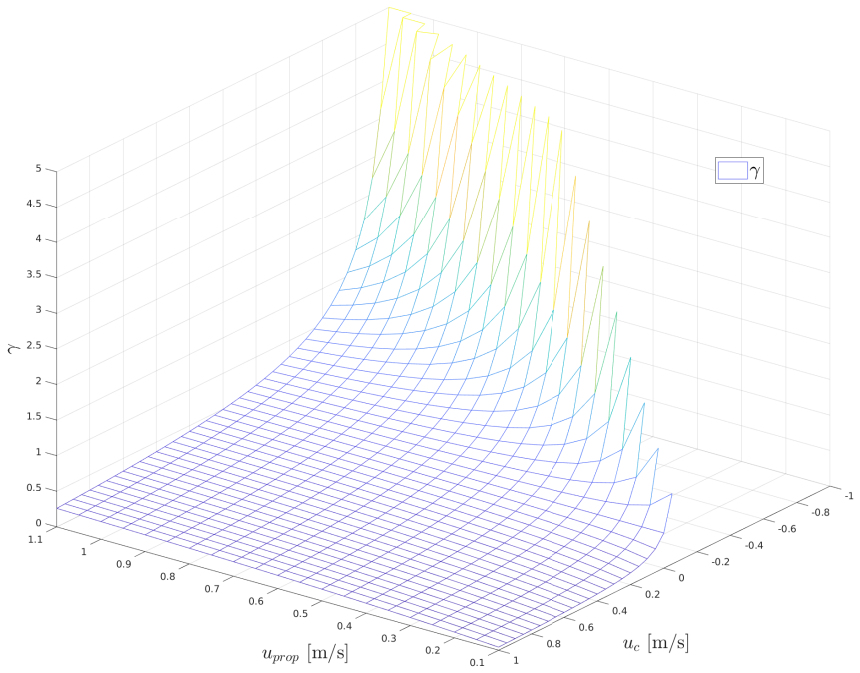

Figure 4: Example of γ as a function of u_{prop} and u_c.

the dynamics changes with variations in sea state (u_{prop}) and current (u_c), we assume $v_c = 0$ and show the family of transfer functions $H_{ql}(s)$ in Figure 3, where $u_c \in [-1, 1]$ m/s and $u_{prop} \in [0.1, 1.1]$ m/s. Due to the combined effects of order of magnitude variations in both u_r and U, we conclude by comparing Figure 3 with the nominal case in Figure 2 that one can expect gain variations between -50 dB and +20 dB compared to the nominal model. At the same time, the variations in phase up to 60° are observed. The cases with increased gain correspond to conditions where the ground speed U becomes very small, while cases with decreased gain correspond to situations where the propulsion speed $u_{prop} = u_r$ is very small (e.g., due to the wave propulsion becoming ineffective in sea states with very small waves and/or waves from the side).

The main variations in dynamics are due to the parameter γ that influences the gain in the Nomoto model (29). We show how γ varies as a function of u_{prop} and u_c in Figure 4. Note that the parameter γ is infinite along the line $u_c + u_{prop} = 0$, which corresponds to the singularity $U = 0$. Figure 5 indicates that it is indeed the gain γ that is the main cause for the variations, where the normalized transfer function $\frac{1}{\gamma} H_{ql}(s)$ is shown. For reference, Figure 6 plots $H_{ql}(s)/H_n(s)$, which indicates that the Nomoto model with parameter-dependent gain is an accurate approximation at high frequencies, while its magnitude deviation is reduced by up to 14 dB at lower frequencies, and phase deviation still up to 60°.
This indicates that course-keeping control should consider the variations in the gain γ, and counteract the disturbances due to winds and current. The latter can be obtained by integral action, since the current, wind and propulsion speeds can be expected to be slowly time-varying variables.

Gain-scheduling based on γ is in principle an interesting approach as illustrated by the above mentioned analysis that shows that the main influence on the transfer function from rudder angle to course angle is captured by the scalar parameter γ. The linear control design approach that is the basis for gain-scheduled (quasi-linear) control is justified by the observation that the main nonlinearities are resulting from the slowly time-varying environmental parameters (winds, waves and current) as well as the course angle command. However, the prospects of a practical realization of a gain-scheduling strategy is limited by the following

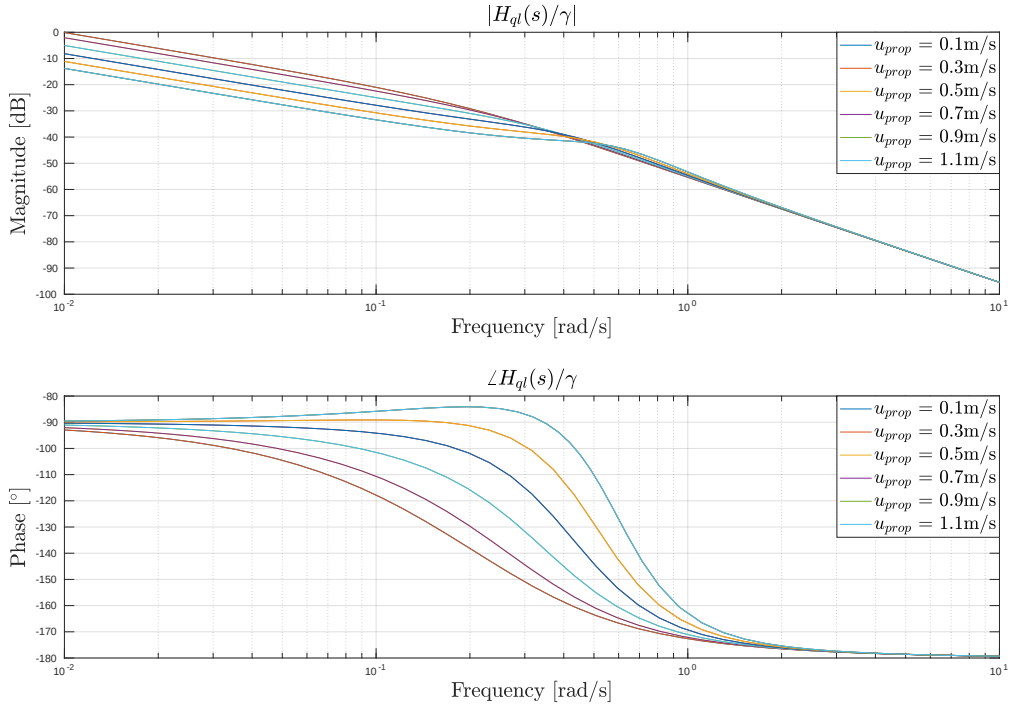

Figure 5: Normalized with γ: Transfer function $H_{ql}(s)/\gamma$ for third-order quasi-linear model when $u_c \in [-1, 1]$ m/s and $u_{prop} \in [0.1, 1.1]$ m/s.

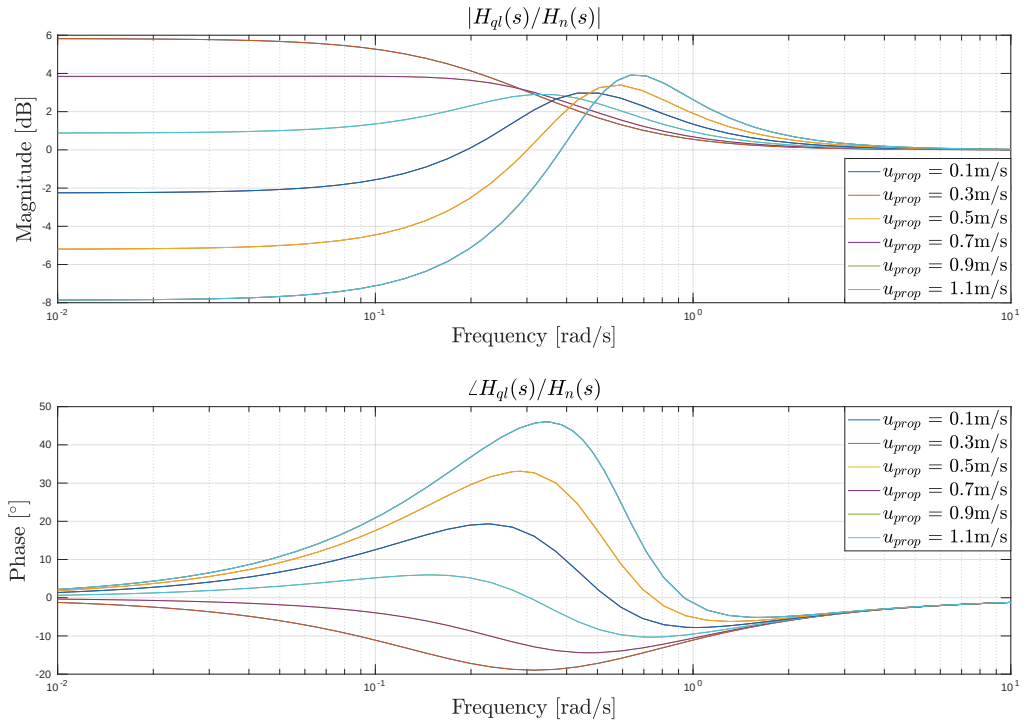

Figure 6: Ratio between the transfer functions of the quasi-linear third-order model and the Nomoto model with nonlinear gain $H_{ql}(s)/H_n(s)$, when $u_c \in [-1, 1]$ m/s and $u_{prop} \in [0.1, 1.1]$ m/s.

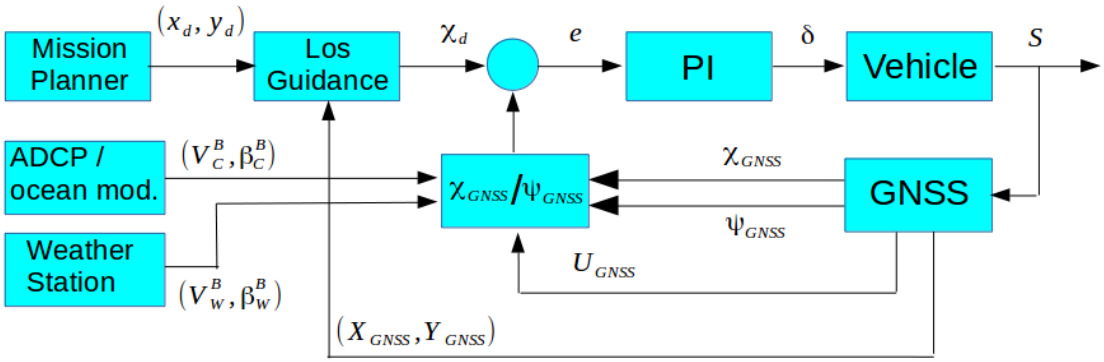

Figure 7: USV's control architecture: the LOS guidance system computes a desired course to the target location (X_d, Y_d), provided by the Mission Planner, based on the vehicle position (X_{GNSS}, Y_{GNSS}) measured from the USV's state S; rudder/course control is achieved measuring the current vehicle's course (χ_{GNSS}) or heading (ψ_{GNSS}), based on the measured ground speed (U_{GNSS}). Course or heading control is chosen depending on SOG, wind and ocean current information measured onboard the USV.

facts:

- The parameter γ depends on the ocean current, which may not be known. It should be kept in mind that although USVs could be equipped with an acoustic Doppler current profiler (ADCP), such an instrument is expensive, power hungry, and results may be inaccurate due to its proximity to the sea surface and the USV's pitching/rolling motions.
- Increasing the gain may not be very effective due to saturation of the rudder angle.
- There is a singularity with infinite γ when U goes to zero, which may be unavoidable due to the limited propulsion that makes the vehicle uncontrollable when the wind or current are too strong compared to the wave propulsion force.
- The course angle may not be reliably measured with the global navigation satellite system (GNSS) when U becomes close to zero, and is in fact undefined at the singular point $U = 0$.

We therefore propose a linear course controller that is robust over a range of environmental conditions, with a switch to a heading controller in case U becomes close to zero or the forward propulsion speed becomes negative. Due to the slowly time-varying nature of the quasi-linear model, a robust linear course controller should be designed with acceptable performance for any constant environmental parameters and course angle command for which U is sufficiently far from zero. In compliance with a preliminary analysis of the vehicle steering model (Dallolio et al., 2019), the implemented autopilot is a linear PI-controller, and its parameters are robustly tuned for $U \geq 0.2\ m/s$. This strategy is evaluated in field experiments as described in the next sections.

4 Experimental results and discussion

Sea trials are carried out in both the Trondheim fjord and off the coasts of Norway in the North Atlantic Ocean. The USV's desired rudder command is computed by a Beaglebone Black[2] microcontroller unit (MCU) that runs DUNE (Pinto et al., 2013), a runtime environment for unmanned systems. Table 4 of Appendix C contains information about the onboard GNSS navigation and weather station systems.

[2]https://beagleboard.org/black

Figure 7 depicts the USV's control architecture and shows how the GNSS is used to close the outer path control loop and the inner course control loop. The choice of controlling the course or the heading of the USV is based on measured currents (from ADCP or ocean models), winds (from weather station) and USV's ground speed. An example of how this logic is employed in the field is shown in Section 4.2. Autonomous path following is achieved via line-of-sight (LOS) guidance system that computes the desired course over ground that steers the vehicle towards the desired path (Fossen, 2021).

4.1 Experimental control: basic results

In the following experiments (Section 4.1.1 and 4.1.2) we demonstrate basic control results obtained in fjord and ocean waters respectively. In both experiments the USV's course is controlled by a PI-controller with gains $K_p = 1.25$ and $K_i = 0.02$, tuned experimentally.

4.1.1 Autonomous navigation in the Trondheim fjord

Fast and irregular waves are expected in fjords, where a reduced wind fetch generates short-crested waves whose amplitude and frequency are mainly dependent on the local wind speed. We therefore expect the vehicle speed to be affected by a combination of sea currents, waves and wind. The USV was commanded to follow a sequence of waypoints disposed in a way that the intended path would create a square and expose the vehicle to different angles relative to the aforementioned disturbances. The mission site is strongly affected by tidal currents with direction and intensity depending on the time of the day. At the time of the mission, low tide generated currents from South-East and the observed mean wave amplitude was approximately 1 meter. The effects of the current can be observed in Figure 8, where it is clear that the USV ground speed U_{GNSS} is higher when it navigates North and West. Figure 8 also shows that the ground speed drops significantly when the vehicle turns into the wind and finds sea currents on its starboard side. In the fourth leg of the trajectory (i.e., from time $t = 5500s$), the ground speed increases due to a combination of wind and current forces in the direction of the vehicle's heading. However, the USV's velocity remains quite high when it enters the last section of the mission. From this we conclude that surface currents have a greater impact than winds on the ground speed and that some forward propulsion is ensured as long as waves are present. From Figure 8 we also conclude that the chosen PI-controller shows a degree of robustness that is good enough to steer the vehicle through the desired waypoints. The bottom graph shows the rudder angle commanded by the course autopilot where it is clear that the contribution of the integral action produces an average constant offset in the commanded rudder angle allowing the USV to keep the average course error within 10°. More wave-induced course and rudder oscillations are however observed in the third leg (from time $t = 3000s$ to $t = 5500s$), where the vehicle heads into the sea currents. The proportional action of the course controller allows indeed larger rudder oscillations meant to correct for the course error. This is in agreement with the linear analysis since the reduced ground speed leads to a higher gain γ in the response from rudder to course, which leads to less stability margins and more oscillations. The field-tested PI course controller proves itself capable of controlling the USV course when the forward propulsion due to waves exceeds the magnitude of environmental forces. Additionally, it is demonstrated that standard integral action is enough to compensate for environmental disturbances.

4.1.2 Autonomous navigation in the North Atlantic Ocean

The same controller was tested in ocean waters, where more regular (i.e., constant in height and frequency over the considered time period) and higher waves are expected as a result of more constant and strong winds. As a consequence, the vehicle propulsion due to waves is also expected to be more regular, with variations in ground speed mainly due to wind and ocean current disturbances. The control architecture was tested along the Norwegian North Atlantic coasts, in a site located approximately 40km north of the Norwegian islands of Frøya and Hitra (mid-Norway). This area is know for quite intense coastal currents from South-West, as a result of the main North Atlantic Current (NAC) hitting the coasts of Norway (Norwegian Current) and continuing North/North-East. In this section we discuss a portion of a 2-weeks mission which lasts for

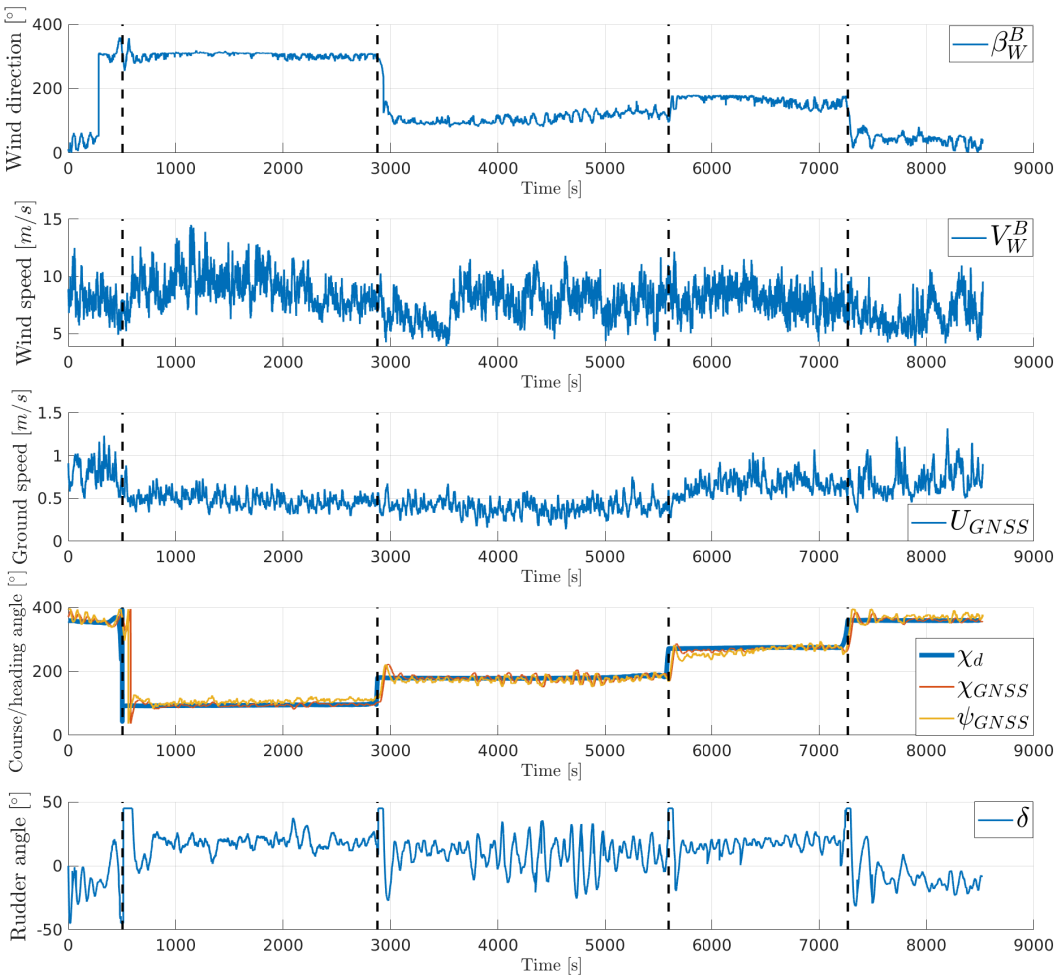

Figure 8: From the top: wind angle in USV body frame (β_W^B); wind speed relative to the USV (V_W^B); vehicle ground speed (U_{GNSS}); desired course (χ_d) and measured course over ground (χ_{GNSS}) and measured heading (ψ_{GNSS}); commanded rudder angle (δ). Black dashed lines indicate waypoint change.

approximately one day.

Figure 9 shows that the absolute wind direction varies significantly (variations up to 120°) in the first hours of the mission, while it becomes more stable before the USV reaches the first waypoint and thereafter. The wind speed is very low in the first part of the mission, and keeps increasing steadily up to approximately 5 m/s in average in the first hours of June 16th. The wind speed increase is followed by an increase of the USV's ground speed that stabilizes around 0.75 m/s halfway between the first and second waypoint. Later during the same day we observe again a wind speed drop and increase, both somewhat correlated with the vehicle's ground speed. Figure 9 also compares measured heading (ψ_{GNSS}) and course over ground (χ_{GNSS}) to the desired course (χ_d) between the waypoints. In the first leg of the mission we observe a course error always within 10° and an average positive rudder angle with oscillations of 15° mean amplitude, meaning that the despite its lowest speed the wind is the main disturbance the integral action compensates for. The wind speed increase impacts the course control, that shows larger oscillations (with amplitude within 20°) around the desired course due to a combined effect of enhanced ground speed and rudder oscillations (up to

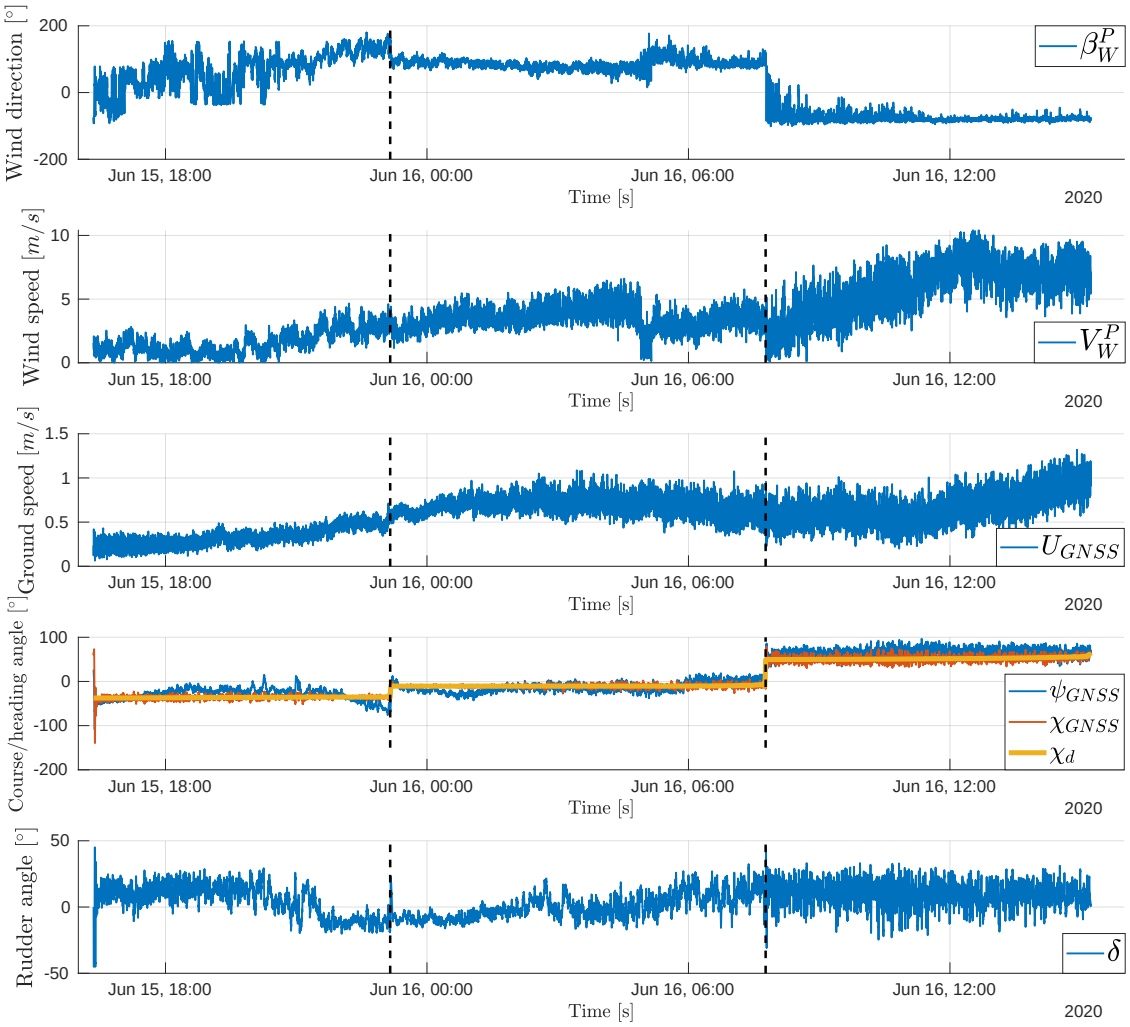

Figure 9: From the top: wind direction (β_W^P) relative to North; wind speed relative to the vehicle (V_W^P); vehicle ground speed (U_{GNSS}); comparison between the measured heading (ψ_{GNSS}) and course (χ_{GNSS}), and desired course (χ_d); commanded rudder angle (δ). Black dashed lines indicate waypoint change.

25°) observed after the second waypoint. Again, rudder oscillations of amplitude below 15° are commanded to compensate for first-order wave-induced vehicle motions, while larger oscillations are commanded to compensate for the wind gusts blowing on the USV port side and that have an immediate effect on the vehicle turning rate r. Moreover, the USV speed increases while moving North-East due to the additional speed provided by the ocean current that moves in the same direction. Overall, the course controller proves itself capable of rejecting the natural disturbances that act against its course-keeping capabilities.

4.2 Experimental control: adverse environmental disturbances

In this section we study the limitations of this course control approach and show situations in which the magnitude of environmental forces exceeds that of the propulsion system, leading to navigation instability. In most cases, loss of course controllability coincides with a loss of speed. The course over ground is defined only when the ground speed is greater than zero, when the latter drops significantly the course measurement provided by the GNSS system becomes unreliable. Most importantly however, if the ground speed drop coincides with a decrease of the USV's speed relative to water (i.e., when the current speed is low), the rudder becomes incapable of exerting a significant steering force. In such situations the closed-loop system

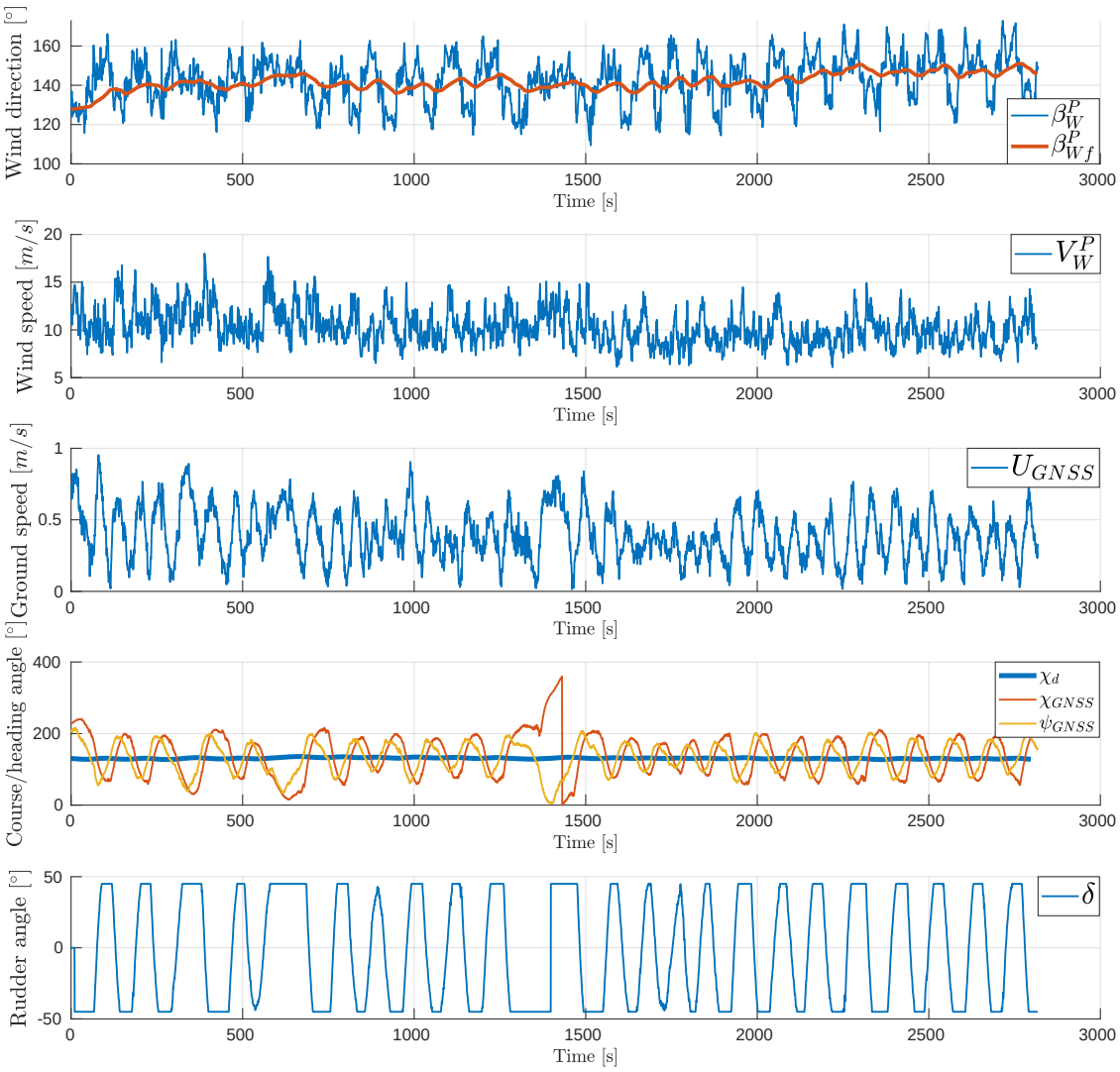

Figure 10: Top: wind direction (β_W^P) and filtered wind direction (β_{Wf}^P) relative to North; absolute wind speed (V_W^P); measured ground speed (U_{GNSS}); comparison between the measured heading (ψ_{GNSS}) and course (χ_{GNSS}), and desired course (χ_d); commanded rudder angle (δ).

(rudder to course) looses its performance as the commanded rudder angle does not generate a significant torque on the vehicle's yaw axis. This phenomenon is also observed when the environmental disturbance (e.g., wind or sea surface current) generates a force that balances the forward propulsion force produced by the submerged hydrofoils.
In this paragraph we analyse two situations in which environmental forces prevent the vehicle to navigate in the intended direction, leading to large course oscillations and eventually total loss of control.

4.2.1 Upwind control experiment

This field experiment took place in enclosed waters within the archipelago of Froan, which separates the coasts of mid-Norway from the North Atlantic Ocean. There the USV was commanded to navigated straight into the wind, which came from South-East with a speed between 10 and 12 m/s in average as shown in Figure 10. At the bottom of the figure we can observe the USV's speed over ground, that increases and decreases as the course oscillates around the desired course, which aligns with the wind direction. Figure 10

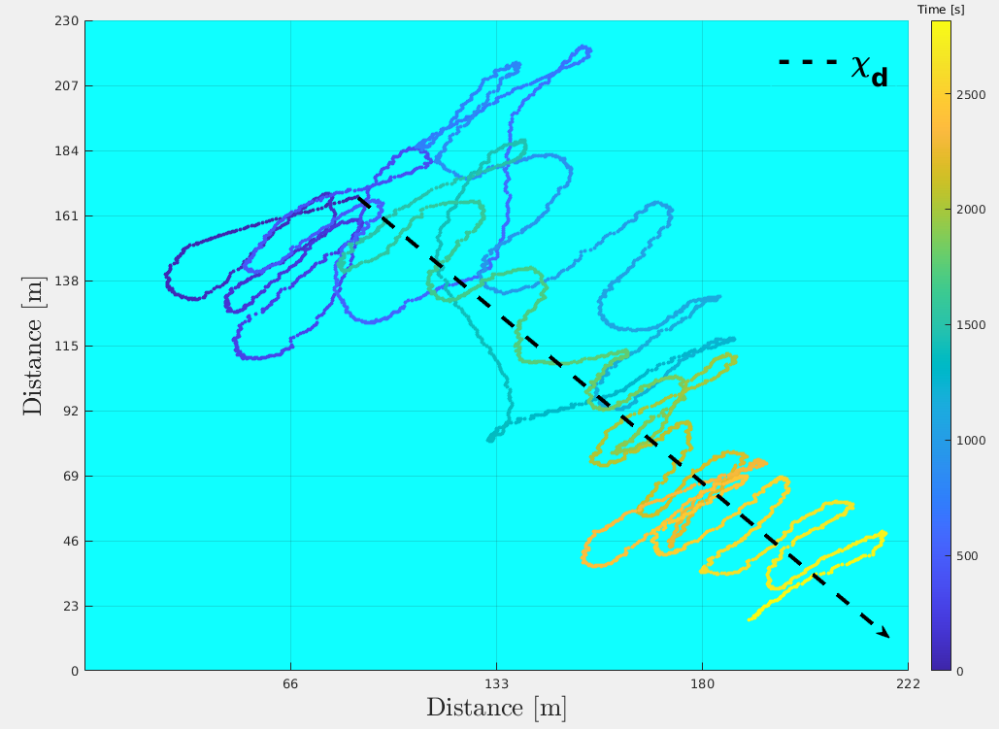

Figure 11: USV's track over time. The black dashed line indicates direction (χ_d) to the target location.

shows that the wind blows from an average direction $\beta^P_{Wf} \approx 140°$, which coincides with the intended vehicle's course (χ_d) as observed in the fourth plot of Figure 10. The signal β^P_{Wf} is obtained after low-pass filtering β^P_W with a time constant $t_f = 100s$. From this we also notice that heading and course oscillations have a similar amplitude of approximately 60°. The last graph of Figure 10 clearly shows that the course controller introduced in Section 4.1 is not capable to keep course control without significant course oscillations. This situation is observed, as expected, when the vehicle's speed over ground decreases towards zero as a result of the wind exerting a force on the USV that balances (or exceeds) its propulsion. This in turn makes the rudder ineffective and the integral error accumulates fast as the commanded rudder angles does not produce a yaw momentum on the vehicle and hence a course change. Moreover, at time $t = 1600s$ the onboard software switches to a P controller with gain $K_p = 1$, as an attempt to reduce the amplitude of oscillations by removing integral effects, at the expenses of the USV's turn rate. Smaller oscillations are indeed observed until time $t = 1800s$, where the amplitude observed is the same as with the initial controller. This indicates, in addition, that the course is not controllable when the ground speed approaches zero. Figure 11 shows the track covered by the USV, characterized by numerous oscillations and a very inefficient navigation towards the desired location.

4.2.2 Heading control switch experiment

This experiment took place in Frohavet, located North-East of the island Frøya and separated from the North Atlantic Ocean by the Froan archipelago. Frohavet is typically affected by full scale oceanic winds, whereas waves and sea currents show lower intensity thanks to the archipelago shielding. Since the effects of the North Atlantic Current are filtered by the Froan islands, major currents components are due to tides. In this example we show a situation in which with total loss of vehicle's controllability, caused by a combined action of wind and sea currents that cause a significant ground speed drop. In this experiment, the USV navigates towards a location North-West of its initial position with the same nominal PI gains of Section 4.1. Figure 12 shows that the vehicle is asked to head straight into the wind, which has initially an average speed of 9 m/s. The USV ground speed in the initial part of the considered period oscillates

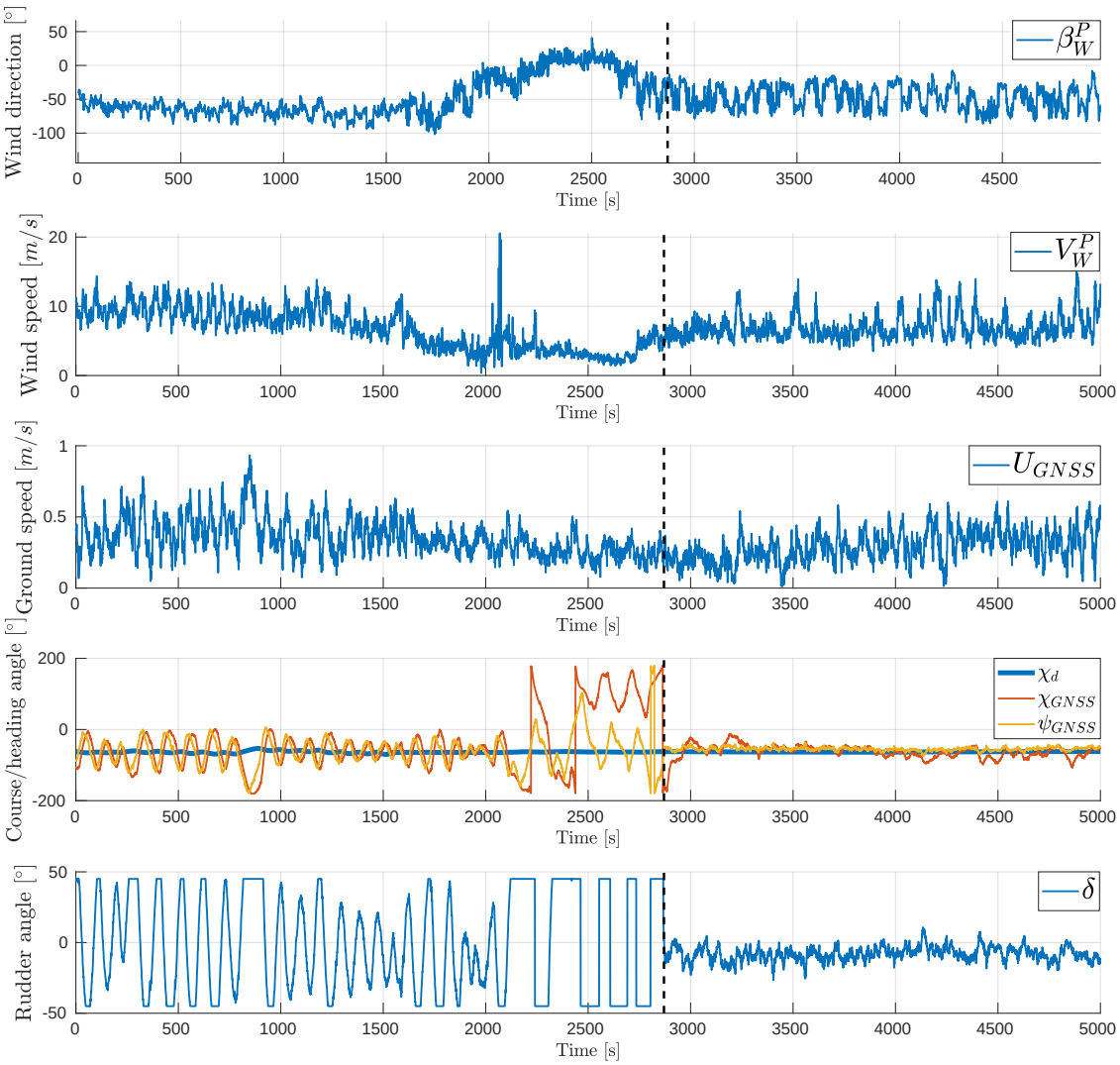

Figure 12: From the top: wind direction (β_W^P) relative to North; absolute wind speed (V_W^P); measured ground speed (U_{GNSS}); comparison between the measured heading (ψ_{GNSS}) and course (χ_{GNSS}), and desired course (χ_d); commanded rudder angle (δ). The black dashed line indicates switch to heading control.

significantly (between 0.1 and 0.8 m/s), suggesting the presence of related course and heading oscillations. The wind speed decreases over time, causing a ground speed similar drop most likely due to the presence of smaller waves. Figure 12 shows in fact large course oscillations of approximately 60° amplitude from the very beginning. As the USV keeps moving with oscillatory course towards the desired location, the effect of tidal currents increases causing the speed over ground to drop even further (around 0.1 m/s). At time $t = 2100s$ the current takes over the vehicle, which spins around and looses its course control stability. At time $t = 2870s$ the onboard software switches from course control to heading control, closing the control loop with the GNSS-provided measurement ψ_{GNSS} instead of χ_{GNSS}. The heading control parameters are relaxed ($K_p = 1$ and $K_i = 0.01$) in order to produce a less aggressive steering control action. Immediate effects can be observed in the commanded rudder signal in Figure 12, whose oscillations and saturation are suppressed. As a consequence the vehicle's heading stabilizes around the desired reference (now a heading angle). Also the course over ground stabilizes with a larger error to the desired heading, indicating that the forces exerted on the USV by the environment are efficiently suppressed with integral action.
Figure 13 shows the complete track covered by the USV. It can be observed that when the autopilot tries to control the course over ground (blue curve), the USV oscillates around the desired path (black dashed

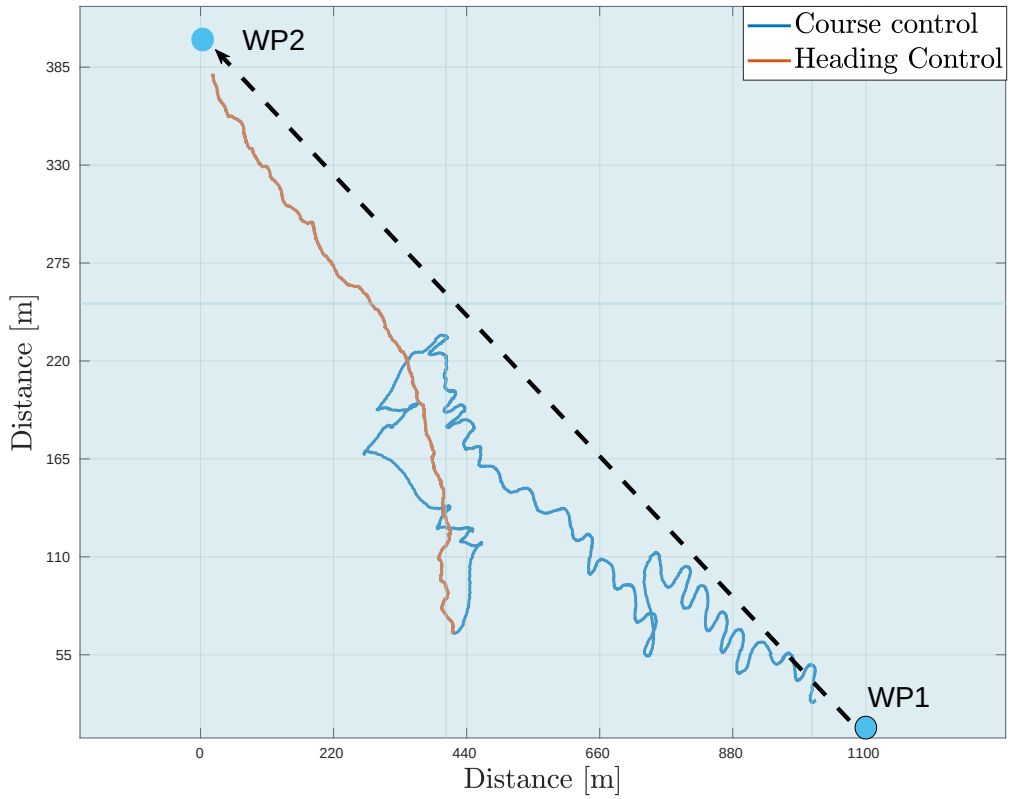

Figure 13: USV track over time: course over ground control (blue) and heading control (red). The black dashed line indicates the vehicle's desired path between the two waypoints.

line) connecting the two waypoints and eventually drifts away from it. When the autopilot switches to heading control (red curve) the USV's course becomes more stable as a result of oscillations suppression. Additionally, the vehicle navigates towards the desired location more efficiently.

4.3 Experimental model validation

In this section we present the validation of the full nonlinear model given by (5)-(8) and of the simplified quasi-linear model given by (28). As the quasi-linear model is valid on specific premises (i.e., straight line navigation) and is obtained by applying some assumptions to the full nonlinear model, we expect this model to perform worse than the full nonlinear model during turns. The validation is carried out using the data collected onboard the USV during sea-trials in the Trondheim fjord. Information on sea currents speed and direction, and waves (height and frequency) are instead obtained from the weather forecast service NorKyst-800[3]. For the purpose of model validation we use a constant propulsion force (F_{prop}) in our simulations. The propulsion force is set such that the average surge velocity u in the simulation matches the average surge velocity of the USV during the sea trial. In reality, as the propulsion depends on waves, variations in propulsion force and USV's ground speed should be expected. As discussed in Section 3, sea currents have a large impact on the vehicle's course dynamics. The turning rate r (8) is indeed directly affected by currents as these modify both the Munk moment as well as the force that the rudder is able to exert on the water mass. The Munk moment has destabilizing effects due to quadratic velocity terms which can be positive and negative (Fossen, 2021).
The validation consists in simulating the USV's dynamics with the same wind and sea current disturbances, and comparing the response of the simulated vehicle after step-wise changes in the desired course.

[3]https://imr.brage.unit.no/imr-xmlui/handle/11250/113865

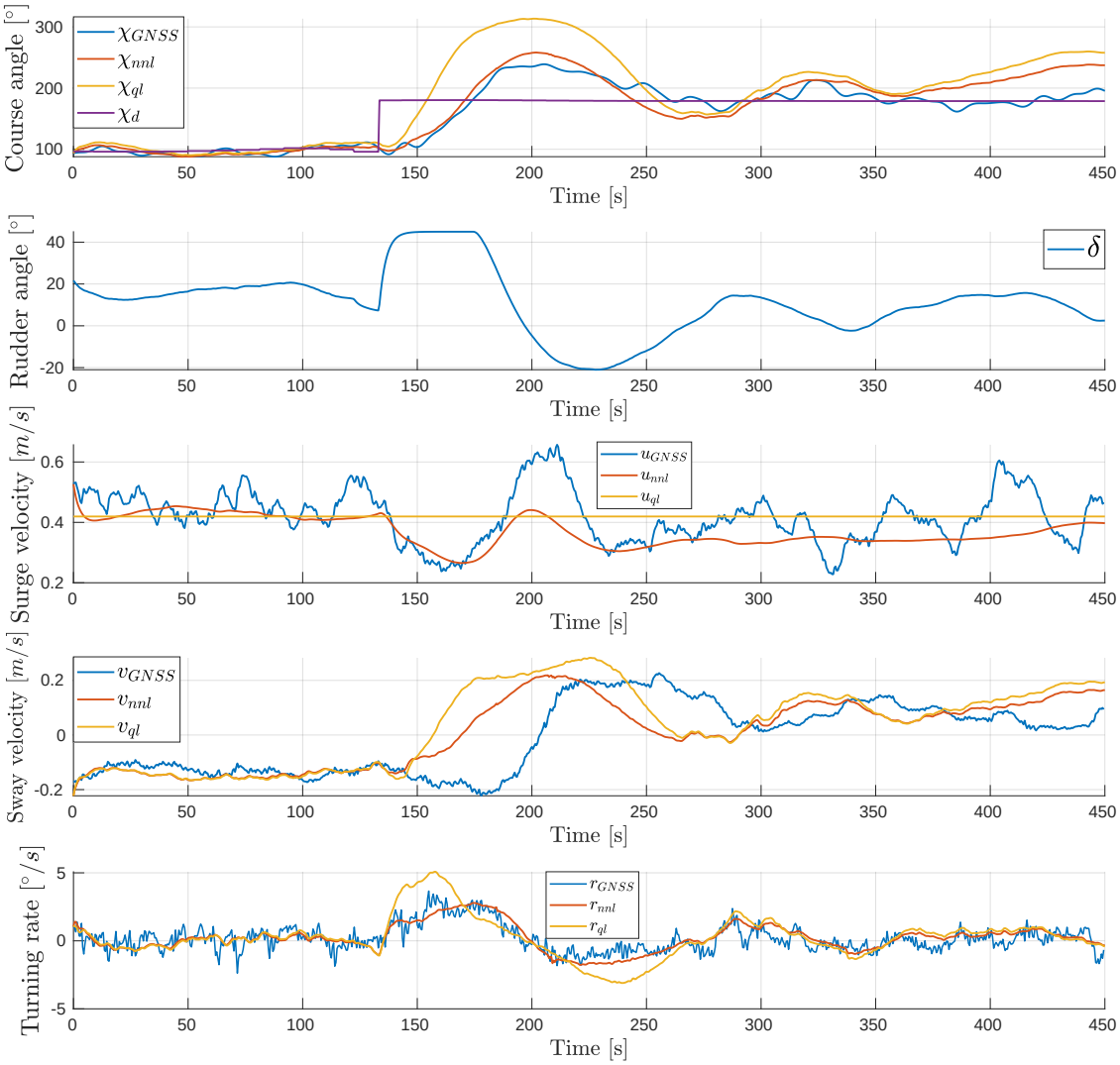

Figure 14: From the top: simulated courses from the full nonlinear and quasi-linear models (χ_{nnl},χ_{ql}), measured (χ_{GNSS}) and desired course over ground (χ_d); rudder signal (δ) used during the field test and fed to the models; full nonlinear model (u_{nnl},v_{nnl},r_{nnl}), quasi-linear model (u_{ql},v_{ql},r_{ql}) and measured states (u_{GNSS},v_{GNSS},r_{GNSS}).

In the sea trials the rudder was controlled by the same PI-controller with gains mentioned in Section 4.1. In this validation we run both open- and closed-loop simulations. In the open-loop simulations the measured rudder angle from the sea trials is input to the model. In the closed-loop simulations the controller is included in the simulator to compute the rudder angle.

4.3.1 Open-loop model validation

Figure 14 compares the measured course over ground (χ_{GNSS}) to the courses simulated with full nonlinear model (χ_{nnl}) and the quasi-linear model (χ_{ql}). It can be observed that the simulated courses resemble the measured USV's course. When the step in the desired course happens the course response of the nonlinear is nearly identical, while it shows some under-damping before stabilizing. The course of the quasi-linear model resembles closely the measured one during straight line navigation, while a larger overshoot is observed during the turn, confirming the premises that make this model valid. Figure 14 also compares the measured vehicle's

states with the full nonlinear and quasi-linear models states. In the first graph we notice that the surge velocity (u_{nnl}) varies less than the actual USV's speed due to the constant propulsion force simplification used in the model simulation. Moreover, given the assumptions made to derive the quasi-linear model, we have chosen a constant surge velocity $u_{ql} = \overline{u}_{GNSS}$. Figure 14 shows that u_{GNSS} increases rapidly at time $t = 200s$. At that point $\dot{u}$ is large and positive, leading to a dampening effect on the course since v is positive (as seen by the last term in (5)). In the simulations however, $\dot{u}$ is smaller and thus the dampening effect is smaller, resulting in the under-damped behaviour. In the quasi-linear model the dampening effect of $\dot{u}$ is completely neglected, which explains the large overshoot. In the same figure it is also observed how waves impact the vehicle's turning rate r. A high-frequency component caused by first-order waves is present in the measured angular velocity r_{GNSS}, while it is not present in the simulated one r_{sim}. An overshoot of r_{ql} is also observed, as a result of the higher USV surge speed u_{ql} when it enters the turn. Overall, the response of r clearly shows that the dominating dynamics are due to the rudder and that the employed models are able to capture them.

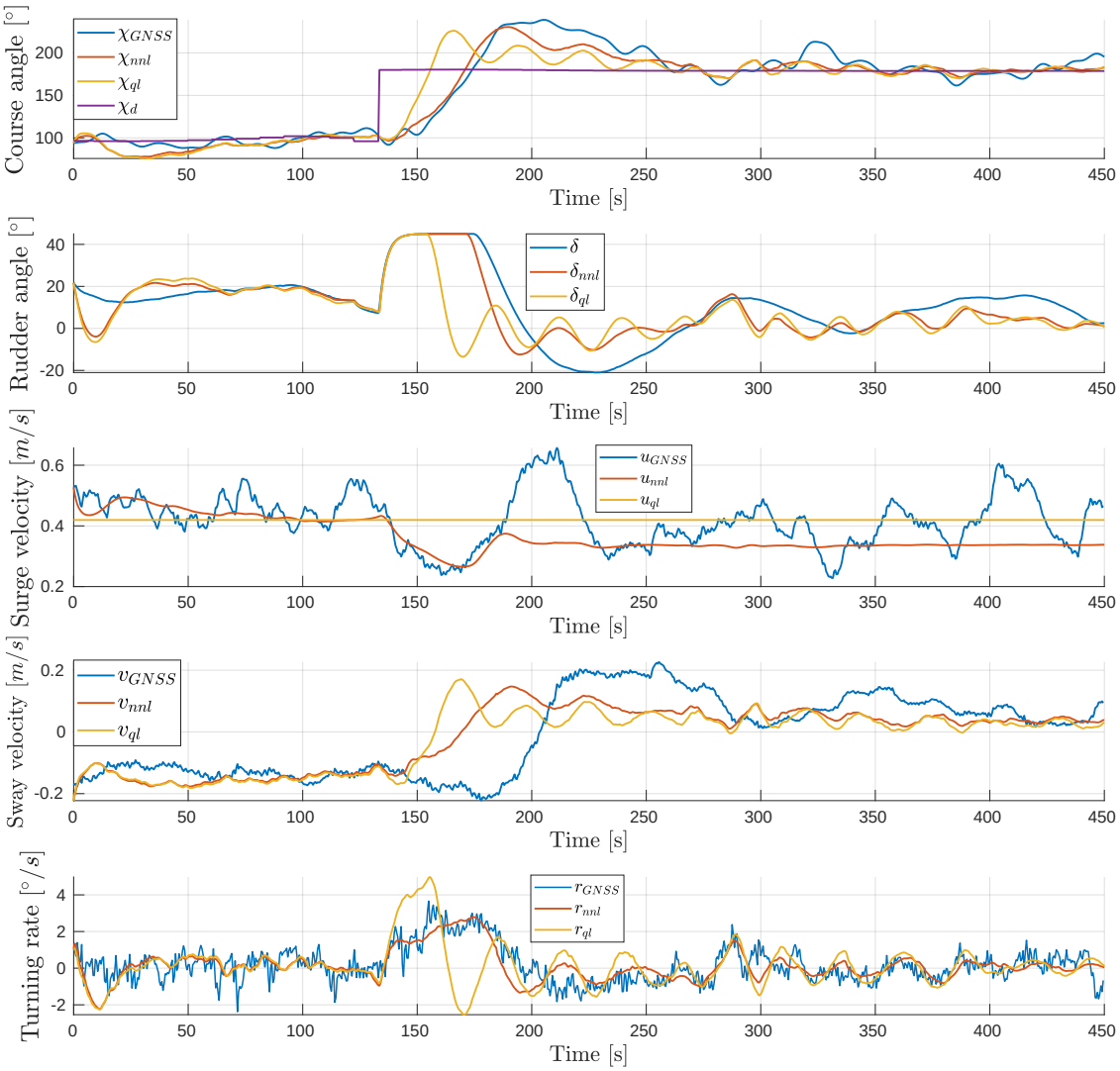

Figure 15: From the top: simulated courses from the full nonlinear and quasi-linear models (χ_{nnl},χ_{ql}), measured (χ_{GNSS}) and desired course over ground (χ_d); rudder signals computed by the simulated autopilots and used as input to each model; full nonlinear model (u_{nnl},v_{nnl},r_{nnl}), quasi-linear model (u_{ql},v_{ql},r_{ql}) and measured states (u_{GNSS},v_{GNSS},r_{GNSS}).

4.3.2 Closed-loop model validation

In this section we analyze the models' stability when the vehicle is controlled by a fixed-gain PI-controller, using the same experimental data of the previous paragraph. This analysis is meant to confirm that the models are still valid when the controller is included in the control loop. The desired vehicle course (χ_d) computed by the LOS guidance during the sea trials is fed to the simulated control loop, for each model. Figure 15 shows the course response of the simulated models compared to the measured course (χ_{GNSS}). It can be observed that the quasi-linear model has a faster course response. This is due to the quasi-linear model overestimating the surge velocity at the moment of turning, as seen in the same figure. This leads to a larger rudder force, seen as an overshoot in the turn rate r in Figure 15, and therefore a faster response. In comparison, the nonlinear model has a surge velocity closer to the measurement and both the course response and turn rate r closely resemble the true measured course during the turn.
When the assumptions of the quasi-linear model becomes invalid during the turn, the gains of the controller are no longer suitable, resulting in oscillations in the course after the turn. The integrator in the controller starts at zero at the beginning of the sea trial and integrates the error. As the integrator state is not an available measurement, its value at any point during the sea trials is unknown. In the simulations we set the initial conditions of the integrator to zero, thus an error can be expected in the initial conditions, resulting in an error at the beginning of the closed-loop simulations. The simulated courses still clearly resemble the measured course, see Figure 15, proving the validity of the presented models.

5 Conclusions

Nonlinear dynamic modeling of a wave-propelled USV has been presented, taking into account the effects of ocean current that may lead to very low speed-over-ground. This includes zero and negative speed-over-ground that lead to singularities.
The models give insight into the changes in steering dynamics as a function of changing environmental conditions, which is exploited in the control design to handle singular situations that occur when the speed-over-ground approaches zero. Classical control design principles based on robust linear course control is used in normal conditions with a sufficiently large speed-over-ground, and with a switch to heading control in the singular conditions.

The presented numerical models highlight challenges and limitations of course-keeping control. This knowledge can be useful for high-level mission planning and decision-making purposes, e.g., a priori knowledge of wind and currents speed and direction might suggest that an alternative route would decrease the travel time to the destination.
In this context, a speed model is key and would provide useful knowledge used for mission planning and course control purposes. The investigation of a speed model for this unique wave-propelled USV is left as a future work.

The nonlinear model, the linearized model analysis, and the control design, are all validated using field experimental tests. The controller has been operational and tested at several sites both in the open ocean and coastal environments for about 7 weeks in total. Selected results have been presented to show the practical performance on the control system.

The model frequency analysis presented in Section 3.2 indicates that gain scheduling based on the variable γ is a viable approach to maintain a stable navigation when the singularity $U = 0$ is approached. Gain scheduling relies however on accurate knowledge of the ocean current, which may not always be a reliable measurement due to uncertainty in the ADCP instrument and ocean models. For this reason we propose a solution in which control performances are kept and eventually improved using the heading measurement from GNSS, which is accurate and reliable at low ground speeds.
Further works will investigate the control approach based on gain scheduling. Eventually, onboard wind and ocean current measurements will be used to adjust the controller's gains, in order to avoid deterioration

of the control performances when the magnitude of environmental forces exceeds the USV's wave-induced propulsion.

A AutoNaut USV model parameters

We define ship and steering model parameters in Tables 1 and 2 accordingly. Computation of the system matrices M, C and D is explained in Section A.1.

Table 1: Vehicle parameters

	Symbol	Value (SI Unit)
Mass	m	250 (kg)
Length at waterline	L_{pp}	4.6 (m)
Beam	B	0.7 (m)
Draught	T	0.15 (m)
Block coefficient	C_b	0.51
Radius of gyration	R_{66}	$0.25L_{pp}$ (m)
CG long. displacement	x_g	0 (m)

Table 2: Steering model parameters

	Symbol	Value (SI Unit)
Rudder area	A_R	0.11 (m^2)
Aspect ratio	Λ	1.68
Rudder coefficient	C_N	1.56
Drag coefficient	t_R	0.3
Force factor	a_H	0.2
Interaction coefficient	x'_H	-1.8
Lateral force coordinate	x_H	-0.4
Longitudinal rudder position coordinate	x_R	-2.3

A.1 System matrices

We employ the method presented by Clarke et al. (1982) to compute the system matrices M. The inertia matrix M is assumed to be constant,

$$M = \begin{pmatrix} 277.7 & 0 & 0 \\ 0 & 462.9 & 0 \\ 0 & 0 & 593.35 \end{pmatrix}. \tag{30}$$

The off-diagonal terms in M are less than 5% of the diagonal terms and are therefore neglected in this model. The Coriolis and centripetal matrix C depend on the relative speed as defined by Equation (3). Therefore the coefficients of C will be recomputed during the simulations.
The damping matrix D is obtained by choosing $D_{11} = M_{11}/T_{surge}$ with $T_{surge} = 2\ s$, $D_{22} = M_{22}/T_{sway}$ with $T_{sway} = 4\ s$ and $D_{66} = M_{33}/T_{yaw}$ with $T_{yaw} = 3\ s$. Consequently,

$$D = \begin{pmatrix} 138.85 & 0 & 0 \\ 0 & 115.73 & 0 \\ 0 & 0 & 197.8 \end{pmatrix} \tag{31}$$

The remaining coefficients are computed as: $A_{11} = M(1,1) - m = 27.73$, $A_{22} = M(2,2) - m = 212.9$, $A_{66} = M(3,3) - J_z = 262.72$ where $J_z = mR_{66}^2 + mx_g^2 = 330.62$.

A.2 Wind model

Wind creates forces in surge F_{Xw} and sway F_{Yw}, and a moment in yaw N_{Zw}. According to Fossen (2021), surge and sway forces generated by the wind are computed as

$$F_{Xw} = \frac{1}{2}\rho_a V_{rw}^2 |C_X(\gamma_{rw}) A_{Fw}| \tag{32}$$

$$F_{Yw} = \frac{1}{2}\rho_a V_{rw}^2 |C_Y(\gamma_{rw}) A_{Lw}|, \tag{33}$$

whereas yaw wind-generated moment is expressed as

$$N_{Zw} = \frac{1}{2}\rho_a V_{rw}^2 |C_N(\gamma_{rw}) A_{Lw} L_{oa}|, \tag{34}$$

where the non dimensional wind coefficients C_X , C_Y and C_N are usually computed using $h = 10m$ as reference height and γ_{rw} is the wind angle of attack relative to the bow. For vehicles that are symmetrical with respect to the xz and yz planes, the wind coefficients for horizontal plane motions can be approximated by

$$C_X \approx -c_x \cos(\gamma_{rw}) \tag{35}$$

$$C_Y \approx c_y \sin(\gamma_{rw}) \tag{36}$$

$$C_N \approx c_n \sin(2\gamma_{rw}), \tag{37}$$

where $c_x \in [0.50, 0.90]$, $c_y \in [0.70, 0.95]$, $c_n \in [0.05, 0.20]$.
A_{Fw}, A_{Lw} and L_{oa} are frontal, lateral areas and length overall respectively. Relative speed V_{rw} between vehicle and wind is computed as

$$V_{rw} = \sqrt{u_{rw}^2 + v_{rw}^2} \tag{38}$$

where $u_{rw} = u - u_w$ and $v_{rw} = v - v_w$, while the components of V_w in the x and y directions are

$$u_w = V_w \cos(\beta_w - \psi) \tag{39}$$

$$v_w = V_w \sin(\beta_w - \psi). \tag{40}$$

with V_w and β_w being the wind speed and direction relative to the vehicle (measured onboard), as shown in Figure 16, and is ψ the vehicle's heading. The wind model parameters are reported in Table 3.

Table 3: Wind model parameters

	Symbol	Value (SI Unit)
Wind coefficient	$[c_x, c_y, c_z]$	[0.5,0.7,0.05]
Frontal projected area	A_{Fw}	0.195 (m^2)
Lateral projected area	A_{Lw}	1.5 (m^2)
Length overall	L_{oa}	5 (m)

B Wind and sea current transformations

Figure 16 shows the definition of wind and sea current angles in the USV's body frame, where V_c is the sea current speed, γ_c its angle of attack, β_c the direction relative to the vehicle. As mentioned in A.2, ψ the vehicle's heading.

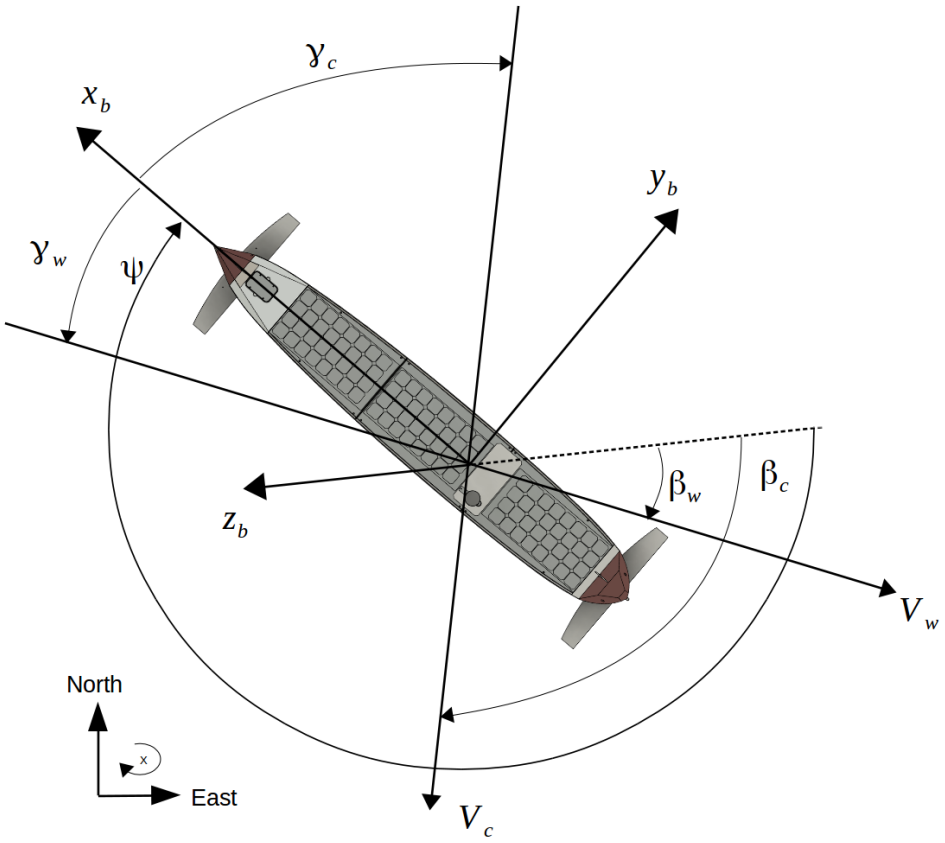

Figure 16: Wind and sea current angles definitions in body frame.

B.1 Sea current to body frame

The sea current is normally defined in polar coordinates (Figure 16). The North-East-Down (NED) components of the current are obtained as

$$N_c = V_c \cos \beta_c \quad (41)$$

$$E_c = V_c \sin \beta_c. \quad (42)$$

The current longitudinal and lateral components in the USV's body frame are then obtained as

$$\begin{pmatrix} u_c \\ v_c \end{pmatrix} = \begin{pmatrix} \cos(\psi) & -\sin(\psi) \\ \sin(\psi) & \cos(\psi) \end{pmatrix} \begin{pmatrix} N_c \\ E_c \end{pmatrix}. \quad (43)$$

B.2 Wind to Earth frame

The onboard weather station (Table 4) measures the wind velocity (V_W^B) and direction (β_W^B) relative to the USV's body frame. Using the measured ground velocity (U_{GNSS}) of the vehicle we can compute the theoretical wind speed (V_W^T), which is the wind speed the USV would perceive if it was stationary:

$$V_W^T = \sqrt{{V_W^B}^2 + U_{GNSS}^2 - 2V_W^B U_{GNSS} \cos \beta_W^B}. \quad (44)$$

Given the low ground speed of the USV, relative and theoretical winds have often similar values. Additionally, we note that the theoretical wind speed is already the absolute (true) wind speed: $V_W^T = V_W^P$.

Using the measured vehicle's heading (ψ_{GNSS}), the absolute (true) wind direction (β_W^P) is simply computed as:

$$\beta_W^P = \psi_{GNSS} + \beta_W^B. \tag{45}$$

C USV navigation payload

Table 4 contains the sensors integrated on the USV. While the GNSS system is mainly used for navigation and control, the weather station collects wind measurements to enhance situational awareness and support high-level control and navigation logic.

Table 4: Navigation sensors

Sensor	Measurement	Frequency
Hemisphere v104s GPS compass[4]	U_{GNSS},χ_{GNSS},ψ_{GNSS},(X_{GNSS}, Y_{GNSS})	2Hz
Airmar 120WX[5]	V_W^B,β_W^B	1Hz

Acknowledgments

This work was supported by the Research Council of Norway (RCN) through the MASSIVE project, grant number 270959, and AMOS grant number 223254 to NTNU.

References

Bowker, J., Tan, M., and Townsend, N. (2020). Forward speed prediction of a free-running wave-propelled boat. *IEEE Journal of Oceanic Engineering*, PP:1–12.

Bowker, J. A., Townsend, N. C., Tan, M., and Shenoi, R. A. (2015). Experimental study of a wave energy scavenging system onboard autonomous surface vessels (asvs). In *OCEANS 2015 - Genova*, pages 1–9.

Camus, L., Pedersen, G., Falk-Petersen, S., Dunlop, K., Daase, M., Basedow, S. L., Bandara, K., Tverberg, V., Pederick, J., Peddie, D., Langeland, T., Cook, J., Kristiansen, T., Tjøstheim, S., Graves, I., Fietzek, P., Sperrevik, A., Christensen, K. H., Sørensen, K., Ghaffari, P., Gramvik, G., Hayes, D., Tassara, L., Aniceto, S., Aune, M., and Dahle, S. (2019). Autonomous surface and underwater vehicles reveal new discoveries in the arctic ocean. In *OCEANS 2019 - Marseille*, pages 1–8.

Clarke, D., Gedling, P., and Hine, G. (1982). The application of manoeuvring criteria in hull design using linear theory.

Costa, M. J. and et.al (2018). Field report: Exploring fronts with multiple robots. In *IEEE AUV*, Porto.

Cross, J. N., Mordy, C. W., Tabisola, H. M., Meinig, C., Cokelet, E. D., and Stabeno, P. J. (2015). Innovative technology development for arctic exploration. In *OCEANS 2015 - MTS/IEEE Washington*, pages 1–8.

Dallolio, A., Agdal, B., Zolich, A., Alfredsen, J. A., and Johansen, T. A. (2019). Long-endurance green energy autonomous surface vehicle control architecture. OCEANS 2019, Seattle, Washington.

Fer, I. and Peddie, D. (2013). Near surface oceanographic measurements using the sailbuoy. In *2013 MTS/IEEE OCEANS - Bergen*, pages 1–15.

Ferreira, A., Costa, M., Py, F., Pinto, J., Silva, M., Nimmo-Smith, W., Johansen, T., Sousa, J., and Rajan, K. (2019). Advancing multi-vehicle deployments in oceanographic field experiments. *Autonomous Robots*, 43.

Fossen, T. (2021). *Handbook of Marine Craft Hydrodynamics and Motion Control, 2nd edition, Wiley.*

Fujii, H. and Tsuda (1962). Experimental researches on rudder performance. (3). *Journal of Zosen Kiokai*, 1962:105–111.

Hine, R., Willcox, S., Hine, G., and Richardson, T. (2009). The wave glider: A wave-powered autonomous marine vehicle. In *OCEANS 2009*, pages 1–6.

Johnston, P. and Poole, M. (2017). Marine surveillance capabilities of the autonaut wave-propelled unmanned surface vessel (usv). In *OCEANS 2017 - Aberdeen*, pages 1–46.

Kijima, K., Nakiri, Y., Tsutsui, Y., and Matsunaga, M. (1990). Prediction method of ship manoeuvrability in deep and shallow waters. In *Proceedings MARSIM & ICSM 90 (1990)*.

Manley, J. and Willcox, S. (2010). The wave glider: A persistent platform for ocean science. In *OCEANS'10 IEEE SYDNEY*, pages 1–5.

Matsumoto, K. and Suemitsu, K. (1980). The prediction of manoeuvring performances by captive model tests. In *J Kansai Soc Naval Archit Jpn (in Japanese)*.

McGillivary, P., Borges de Sousa, J., Martins, R., Rajan, K., and Leroy, F. (2012). Integrating autonomous underwater vessels, surface vessels and aircraft as persistent surveillance components of ocean observing studies. In *2012 IEEE/OES Autonomous Underwater Vehicles (AUV)*, pages 1–5.

Nomoto, K. (1957). On the steering qualities of ships. *International shipbuilding progress*, 4:354–370.

Pinto, J., Dias, P. S., Martins, R., Fortuna, J., Marques, E. R. B., and de Sousa, J. B. (2013). The lsts toolchain for networked vehicle systems. *2013 MTS/IEEE OCEANS - Bergen*, page 1–9.

Smith, R. N., Das, J., Hine, G., Anderson, W., and Sukhatme, G. S. (2011). Predicting wave glider speed from environmental measurements. In *OCEANS'11 MTS/IEEE KONA*, pages 1–8.

Technologies, L. (2019). C-enduro long endurance asv.

Wang, L., Li, Y., Liao, Y., Pan, K., and Zhang, W. (2019). Course control of unmanned wave glider with heading information fusion. *IEEE Transactions on Industrial Electronics*, 66(10):7997–8007.